frontiers | Frontiers in Astronomy and Space Sciences

ORIGINAL RESEARCH
published: 26 April 2022
doi: 10.3389/fspas.2022.832607

Estimating the Coronal Supra-Arcade Downflow Radio Emission: From Centimeter Through Submillimeter Wavelengths

Ernesto Zurbriggen[1*†], *C. Guillermo Giménez De Castro*[1,2†], *Andrea Costa*[3†], *Mariana Cécere*[3,4†] *and Caius L. Selhorst*[5]

[1]Centro de Rádio Astronomia e Astrofísica Mackenzie (CRAAM), Universidade Presbiteriana Mackenzie, São Paulo, Brazil, [2]Instituto de Astronomía y Física del Espacio (IAFE-UBA), Consejo Nacional de Investigaciones Científicas y Técnicas (CONICET), Buenos Aires, Argentina, [3]Instituto de Astronomía Teórica y Experimental (IATE), Consejo Nacional de Investigaciones Científicas y Técnicas, Córdoba, Argentina, [4]Observatorio Astronómico de Córdoba (OAC), Universidad Nacional de Córdoba (UNC), Córdoba, Argentina, [5]NAT—Núcleo de Astrofísica, Universidade Cidade de São Paulo, São Paulo, Brazil

Supra-arcade downflows (SADs) are infrequent, wiggly, and low-emission structures observed to descend through the solar corona, mostly in EUV and soft X-ray frequencies. Based on their physical characteristics, SADs have been interpreted as low-density bubbles and are related to magnetic reconnection processes during long-term erupting flares. In this work, we use numerical MHD simulations to compute flux density maps, which are convolved with telescope beams to synthesize images with the aim to assess the expected SAD emission in radio wavelengths. We assume that the emission is thermal bremsstrahlung from a fully ionized plasma and without any appreciable gyroresonance contribution since magnetic fields are of the order of 10 G. We find that SAD emission should be optically thin in the frequency range of [10–1,000] GHz, and the spatially integrated flux should be larger than 1 Jy. We conclude, therefore, that SADs consistently are less bright than the surrounding fan and that observing SADs in radio frequencies between [0.5–1,000] GHz is feasible with present instrumentation. The observing strategies are proposed, including the instruments that can be used. Moreover, since the emission is, for the most part, optically thin, the flux density is proportional to temperature, density, and line-of-sight depth and when combined with EUV and soft X-ray images may allow a better density and temperature determination of SADs.

Keywords: sun: corona, sun: flares, sun: magnetic fields, sun: radio radiation, MHD—instabilities

Edited by:
Masumi Shimojo, National Astronomical Observatory of Japan (NINS), Japan

Reviewed by:
Debi Prasad Choudhary, California State University, Northridge, United States
David McKenzie, National Aeronautics and Space Administration (NASA), United States

****Correspondence:***
Ernesto Zurbriggen
ernesto.zurbriggen@craam.mackenzie.br

†ORCID ID:
Ernesto Zurbriggen, orcid.org/0000-0002-3480-7107;
C. Guillermo Giménez De Castro, orcid.org/0000-0002-8979-3582;
Andrea Costa, orcid.org/0000-0002-4369-7392;
Mariana Cécere, orcid.org/0000-0002-9844-0033

Specialty section:
This article was submitted to Stellar and Solar Physics, a section of the journal Frontiers in Astronomy and Space Sciences

Received: *10 December 2021*
Accepted: *02 March 2022*
Published: *26 April 2022*

Citation:
Zurbriggen E, Giménez De Castro CG, Costa A, Cécere M and Selhorst CL (2022) Estimating the Coronal Supra-Arcade Downflow Radio Emission: From Centimeter Through Submillimeter Wavelengths. Front. Astron. Space Sci. 9:832607. doi: 10.3389/fspas.2022.832607

1 INTRODUCTION

In EUV and soft X-ray observations, coronal supra-arcade downflows (SADs) are seen as wiggly, low-emission structures leaving extended dark wakes during their descending motions toward the solar surface till they finally stop and gradually disappear. Often SAD descending motions resemble tadpoles swimming upstream through the fluid interstices that oppose less resistance. SADs have usually been detected during the early decay phases of long-term eruptive flares producing coronal mass ejections occurring many times during the first hour after the peak flare intensity. The SAD typical lifetime is of a few minutes. Today there exists a general consensus

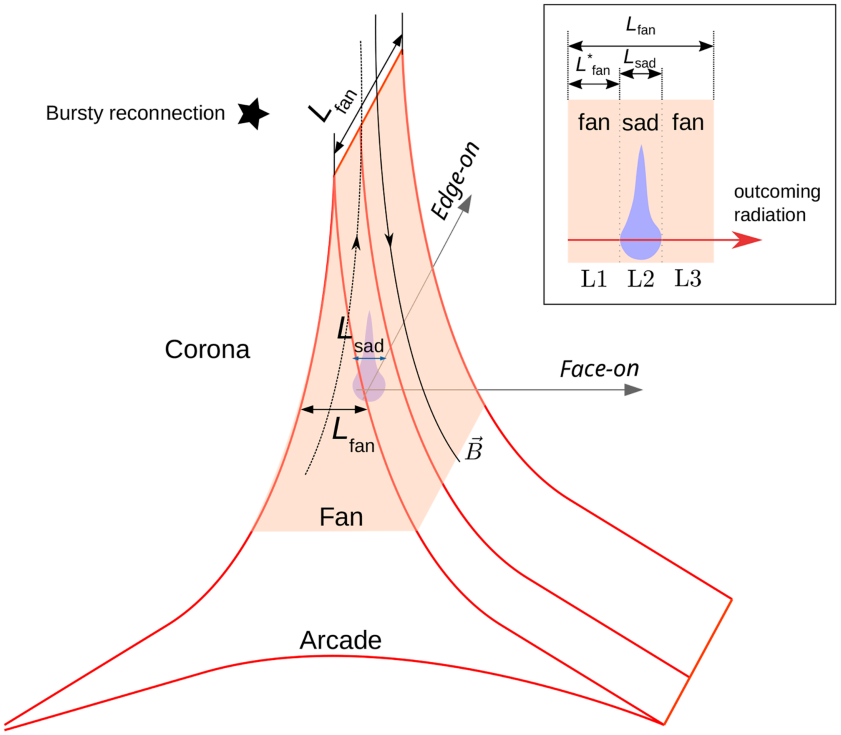

FIGURE 1 | Schematic scenario of a SAD (blue feature) embedded in the bright, hot, and dense fan plasma (shaded region). Below the fan lies the post-flare arcade, and the external coronal medium surrounds it. The fan in addition embeds the expected supra-arcade current-sheet (dark lines with arrows). The fan is represented as viewed by an observer to the limb with two particular line-of-sights of interest represented, the edge-on and face-on views. Given that the fan is a thin, linear, and long structure along the edge-on direction, when the fan is viewed edge-on, the line-of-sight depth L_{fan} is greater than when viewed face-on. (Inset) Sketches a three-layer scheme used to compute the outcoming radiation considering a SAD embedded in the fan for an observer in the arrow direction.

that SADs are subdense cavities of plasma, with densities lower than their surroundings and, thus, having an intrinsically lower brightness (Innes et al., 2003b). SADs have been reported in several events (McKenzie and Hudson, 1999; McKenzie and Savage, 2009; Savage and McKenzie, 2011; McKenzie and Savage, 2011; Warren et al., 2011; Hanneman and Reeves, 2014; Chen et al., 2017) and using different instruments and observational techniques: direct images, with TRACE in EUV and XRT/Hinode and AIA/SDO in soft X-rays; and spectra with SUMER/SOHO in EUV. SADs are observed to descend from the upper part of the fan, a region that lies above the post-flare arcade, which is formed after the eruption, and it is also known in the literature as post-eruption supra-arcade; plasma sheet; thermal halo; supra-arcade fan; or just fan (hereafter used, see the sketch of **Figure 1**). The fan is a dynamical region exhibiting turbulent motions with a relatively high plasma β parameter ($\gtrsim 1$; McKenzie, 2013; Freed and McKenzie, 2018), is bright in EUV and soft X-ray wavelengths, providing the necessary contrast for SAD detection; and is also hotter and denser than the external coronal medium by roughly an order of magnitude. SADs are observed in limb flares and generally when the fan is viewed face-on (i.e., perpendicular to the arcade axis, see **Figure 1**), whereas almost not in edge-on views. On the other hand, soft X-ray observations have provided evidence that the bright plasma of the fan surrounds a current sheet (Liu et al., 2013; Warren et al., 2018) that, in line with the classical model of eruptive flares, is expected to form behind the coronal mass ejection. In addition, there is observational evidence that the current sheet extends high in the corona with the fan just covering the lower part of it.

Despite the fact that several models of SADs have been proposed, the SAD origin and dynamics are not yet completely understood; therefore, the mechanism of their driving physical process is still open to further research. Based on observations and theoretical considerations, a common point among all proposed models is the association of possible SAD origins with post-eruption magnetic reconnection processes occurring inside the fan or in its upper coronal medium (**Figure 1**). Some models (Linton et al., 2009; Longcope et al., 2009; Scott et al., 2013; Guo et al., 2014; Longcope et al., 2018), have pointed out to reconnection downflows descending through the fan as the driven mechanism: considering the standard model of erupting flares, behind the coronal mass ejection, magnetic field lines of opposite polarities are swept together forming the supra-arcade current sheet where the lines reconnect. As a result, part of the reconnection outflows is propelled downward, *via* magnetic tension, to the already-formed underlying arcade, likely in the form of descending magnetic flux tubes or loops. With this picture in mind, Linton et al. (2009), see also Linton and Longcope (2006), carried out 3D MHD simulations considering

an intermittent burst of patchy reconnection in a Y-type current sheet, which supported the idea that SADs are descending reconnected flux tubes. Then, Savage et al. (2012) interpreted SADs as subdense wakes left by shrinking reconnected flux tubes by the observational analysis of one event. In turn, Guo et al. (2014), see also Innes et al. (2014), proposed that reconnected flux tubes in their retracting motions through the inhomogenous fan generate interfaces of plasma where Rayleigh–Taylor instabilities are developed and subsequently generate the SAD phenomenon. In these models, SADs are triggered in the current sheet neighborhood, that is, inside the fan or in its upper coronal region. A common issue with the reconnection downflow interpretation of SADs is the several-time reported discrepancy between the measured SAD speeds (often smaller than 200 km s^{-1}) and the theoretical reconnection downflow speeds, expected to be the Alfvén speed (~1,000 km s^{-1}) of the fan. Among the possible explanations to overcome this speed mismatch, it was proposed that drag forces could act on the descending motion of reconnection downflows (Longcope et al., 2018), slowing them down.

In contrast with the abovementioned reconnection downflow interpretation of SADs, Costa et al. (2009), Schulz et al. (2010), Maglione et al. (2011), Cécere et al. (2012), Cécere et al. (2015), and Zurbriggen et al. (2016) have assumed SADs to be generated by spontaneous, intermittent, and bursty magnetic reconnection processes taking place somewhere in the turbulent-like fan or in its upper coronal region. One of these bursty reconnection events injects energy in a localized fast way, resembling a spark or explosive event, generating shock and rarefaction nonlinear waves, leading to the formation of a subdense cavity, whose structure supports the external pressure because it is hotter than its surroundings, and which is then observed in EUV and soft X-rays as a low-emission structure moving down along the bright fan. These spontaneous reconnection drivers are considered local processes, which could be independent of the overall supra-arcade current sheet. A common characteristic of simulated SADs by Costa et al. (2009) and their subsequent works is that SADs are hotter than the fan. However, some observational studies (Hanneman and Reeves, 2014; Reeves et al., 2017; Xue et al., 2020) have pointed out that SADs are hotter than the upper coronal medium, but they do not seem to be hotter than the fan. This temperature discrepancy between SADs and the fan is due to simplifying assumptions on our modeling, which may be overcome by considering a more complex fan scenario. In addition, a questionable point related to the scenario proposed by Zurbriggen et al. (2016) is that the simulated SADs exhibited lack of elongated tadpole-like shapes during their descent; instead, they showed a more compact shape which opposes several observational reports. This issue is a consequence of considering explicitly anisotropic thermal conduction in the MHD simulations.

Finally, given that SADs are not usually detected during eruptive flares, an important question still remaining to be answered by observations and models is whether SADs are an infrequent phenomenon, and thus, rarely observed, or are they a common phenomenon usually not detected for some reason. SADs have been mainly detected and studied in EUV and soft X-ray frequencies, whereas in radio wavelengths, only indirect evidence have been reported, and, as far as we know, no attempt has been made to detect them directly. In this work, we compute the expected thermal bremsstrahlung emission produced by SADs in wavelengths from centimeter to submillimeter using the numerical MHD models presented by Guo et al. (2014), Cécere et al. (2015), and Zurbriggen et al. (2016). Moreover, we synthesize maps by convolving the telescope beams of the Atacama Large Millimeter/Submillimeter Array (ALMA) in Chajnantor (Chile) and the Karl G. Jansky Very Large Array (VLA) in Socorro (United States) with the MHD simulations of SADs carried out by Zurbriggen et al. (2016). The goal of this work is to motivate and identify the best strategy to observe in centimeter – submillimeter wavelengths these illusive structures triggered during long-term solar erupting flares.

2 REVIEW OF OBSERVATIONS

EUV and soft X-ray observations have reported that the fan is hotter and denser than the background coronal plasma in approximately an order of magnitude, with fan temperatures in the ~[10–20] MK range and ion number densities of ~10^9 cm^{-3}. In an observational study, Hanneman and Reeves (2014) measured plasma temperatures for the fan, SADs, and coronal background in four flare events using differential emission measures, briefly reporting that the peak temperatures of SADs are in the ~[2–12] MK range, with just one SAD being hotter than 10 MK; the fan temperatures are ~10 MK, except a temperature measurement of 20 MK, but having high uncertainty and background temperatures of ~[2–3] MK. In addition, in the literature, we find that SADs have been detected at heights ~[40–150] Mm above the solar surface, with an average height of ~80 Mm; descend distances of ~[10–20] Mm; have downward speeds in the ~[50–500] km s^{-1} range, but with a relatively low average speed of ~130 km s^{-1}; with SAD sizes between ~[1–10] Mm; and have lifetimes of around ~[5–10] min, although there have been few extreme exceptions. On the other hand, the emission contrast between the dark structure and surrounding bright fan is an essential parameter during SAD detection, where, for example, values of ~[2–4] were reported by Xue et al. (2020), see their Figure 4D. Less observational data about SAD properties are available in wavelengths other than EUV and soft X-rays. Among all limb flare events reported in the literature with SAD detection or any signature of their presence, four events extensively studied occurred on 21 April 2002 on the NOAA active region (AR) 9906 (e.g., see Innes et al., 2003a,b; Verwichte et al., 2005); 22 October 2011 on NOAA AR 11314 (McKenzie, 2013; Hanneman and Reeves, 2014; Reeves et al., 2017; Xue et al., 2020; Li et al., 2021); 19 July 2012 on NOAA AR 11520 (Liu, 2013; Liu et al., 2013; Innes et al., 2014); and 10 September 2017 on NOAA AR 12673 (Longcope et al., 2018; Warren et al., 2018; Cai et al., 2019; Hayes et al., 2019; Yu et al., 2020). While the fan view for the first two events was face-on, the view for the third and fourth ones was

edge-on. On the other hand, the fan is a linear-like, long column of plasma along the current sheet direction (edge-on view, see the sketch of **Figure 1**) with ~[3–30] Mm depths, and it is noted that it is considerably thinner in the perpendicular direction (face-on view).

So far, there has not been any direct SAD detection in radio or microwaves at any frequency. On the other hand, some observational studies of limb flaring events (Asai et al., 2004; Chen et al., 2015; Yu et al., 2020), preferably in edge-on views, revealed temporal and spatial correlations between EUV recurring downflow motions in the fan and subsequent detection of impulsive radio emission bursts on the top and/or leg of the lower arcade. In any case, the downflows had a counterpart in radio wavelengths. Assuming the reconnection downflow interpretation of SADs, these authors interpreted the radio impulsive emissions as a consequence of the presence of SADs.

3 MODELING THE EXPECTED EMISSION

3.1 Supra-Arcade Downflow Models Description

In order to calculate the thermal bremsstrahlung emissions of fans and SADs, we need to know their plasma temperatures and densities. Given that these data are not always provided by the models, we circumscribe to the numerical MHD scenarios presented by Guo et al. (2014), Cécere et al. (2015), and Zurbriggen et al. (2016). **Table 1** summarizes the relevant mean characteristics of each model: SAD size $L_{\rm sad}$; SAD (inner) ion number density $n_{\rm sad}$ (also equivalent mass density $\rho_{\rm sad}$) and temperature $T_{\rm sad}$; and fan (outer) ion number density $n_{\rm fan}$, temperature $T_{\rm fan}$, and mean magnetic field intensity $B_{\rm fan}$. Comparing the values of the models listed in **Table 1** and those reported by observations in **Section 2**, it is to be noted that all models predict SAD temperatures higher than the observationally reported ones, whereas the modeled fan temperatures and densities are in agreement with those in observations, except the fan densities of models 2 and 3 that seem to be a bit high.

Following the work of Costa et al. (2009) and motivated by the turbulent-like description of the fan provided by McKenzie (2013), Cécere et al. (2015) carried out 3D ideal MHD simulations to model a turbulent and dynamical fan as the medium where SADs descend. In order to generate this, a combination of tearing-mode and Kelvin–Helmholtz instabilities was used. It was argued that to obtain SADs compatible with observations, the activation of spontaneous bursty reconnection processes is required and that SADs support the external pressure because they are hotter than their surroundings. Moreover, for contrast requirements, Cécere et al. (2015) suggested that there must be a closed relation between SAD sizes and fan widths that should be satisfied for SADs to be observable. For this reason, SADs of two different characteristic sizes were generated with $L_{\rm sad}$ = 4 Mm and $L_{\rm sad}$ = 12 Mm (models 2 and 3 in **Table 1**, respectively).

Considering the scenario presented by Cécere et al. (2015), the 2D MHD simulations of Zurbriggen et al. (2016) considered the particular case of small SADs ($L \approx$ 2Mm), where thermal conduction is expected to be more efficient and SADs fade away much faster than their typical lifetime. In this case, a properly turbulent fan was generated using a stirring force source. **Figure 2** shows images of density (**Figure 2A**) and temperature (**Figure 2B**) maps. The images display three SADs, two strongly faded away due to the thermal diffusion, and the third one at the bottom left corner with coordinates $(x,y) = (-3,-6)\times10^8$ cm and size $\approx$2 Mm $\equiv 2.8''$ is the most intense. This SAD has a mean density $\rho_{\rm sad} \approx 5.1\times10^{-15}$ g cm^{-3}, while the fan is almost three times denser, $\rho_{\rm fan} \approx 1.2\times10^{-14}$ g cm^{-3}. On the other hand, the SAD inner temperature $T_{\rm sad} \approx 19.2$ MK is three times greater than the outer $T_{\rm fan} \approx 7$ MK. This model (model 1 in **Table 1**) represents the case of a fan viewed face-on.

Guo et al. (2014), performing 3D-resistive MHD simulations, generated SADs by means of Rayleigh–Taylor instabilities associated with shrinking motions of magnetic flux tubes. In their scenario, using constant magnetic resistivity, SADs have characteristic sizes within $[6'' - 15'']$ ($\equiv$ [4.7 – 11.6] Mm, see their Figure 2). Therefore, for models 4 and 5 listed in **Table 1**, the extreme values of this size range were adopted, and the remaining values of density and temperature required for our analysis were extracted by visual inspection from their **Figures 2B, C**.

3.2 Expected Total Flux

Hereafter, we will refer to models summarized in **Table 1** as model 1 to the smallest SAD (here considered) taken from the study by Zurbriggen et al. (2016); models 2 and 3 to the small and

TABLE 1 | Summary of relevant mean characteristics of different numerical MHD models. $L_{\rm sad}$ is the SAD size; $n_{\rm sad}$, $\rho_{\rm sad}$, and $T_{\rm sad}$ are the SAD (inner) average ion number densities, equivalent mass density, and temperature, respectively; $n_{\rm fan}$, $\rho_{\rm fan}$, and $T_{\rm fan}$ are the corresponding fan (outer) values; and $B_{\rm fan}$ [G] represents the mean magnetic field intensity of the fan. Data were taken from literature and here referred as model 1 from Zurbriggen et al. (2016); models 2–3 from Cécere et al. (2015); and models 4–5 from Guo et al. (2014).

Model	$L_{\rm sad}$ [Mm]	$n_{\rm sad}$ [cm^{-3}]	$\rho_{\rm sad}$ [g cm^{-3}]	$n_{\rm fan}$	$\rho_{\rm fan}$	$T_{\rm sad}$ [MK]	$T_{\rm fan}$	$B_{\rm fan}$
1	2	2.4×10^9	5.1×10^{-15}	5.8×10^9	1.2×10^{-14}	19.2	7	3
2	4	8.9×10^9	1.5×10^{-14}	20×10^9	3.3×10^{-14}	22.4	10	5.9
3	12	6.5×10^9	1.1×10^{-14}	20×10^9	3.3×10^{-14}	27	10	5.9
4	4.7	2.6×10^9	4.3×10^{-15}	3.3×10^9	5.5×10^{-15}	22	18	14
5	11.6	2.6×10^9	4.3×10^{-15}	3.3×10^9	5.5×10^{-15}	22	18	14

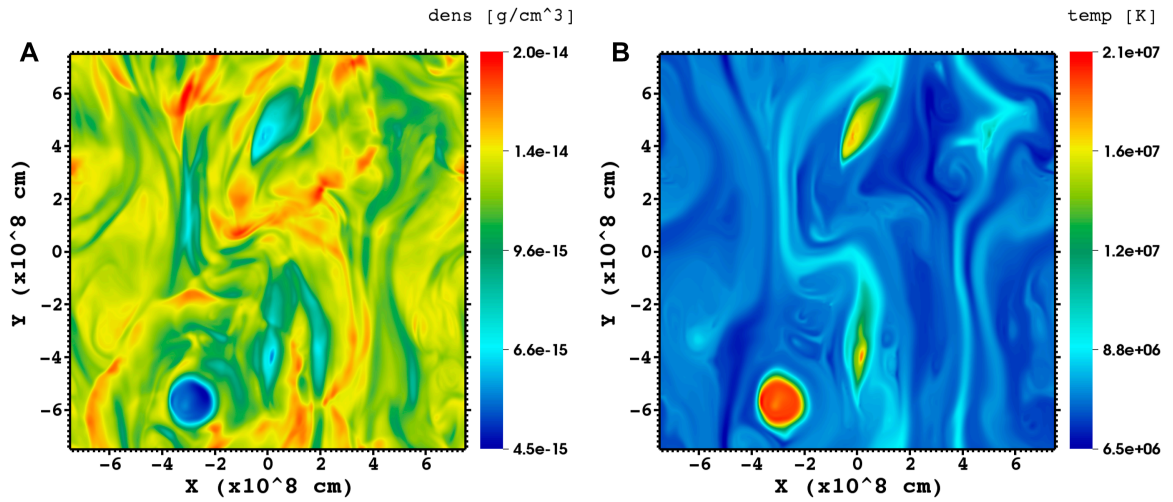

FIGURE 2 | 2D MHD numerical simulation of SADs descending through a turbulent fan explicitly considering thermal conduction (presented in Zurbriggen et al., 2016). **(A)** Density values are shown. **(B)** Corresponding temperature. This model represents a fan viewed face-on. It is to be noted that 10^8 cm ≡ 1 Mm.

big SADs simulated by Cécere et al. (2015); and models 4 and 5 to the extreme sizes (6″ and 15″) reported by Guo et al. (2014).

In order to compute the (free–free) thermal bremsstrahlung emission, we use the expression

$$F(\nu) = \frac{2k_B T \nu^2}{c^2}\left(1 - e^{-\tau_\nu}\right)\Omega \ , \tag{1}$$

where k_B is the Boltzmann constant and c is the speed of light. T_ν is the optical depth at frequency ν, which is approximated by Dulk (1985)

$$\tau_\nu = \kappa_\nu L \ ,$$
$$\kappa_\nu = 9.78 \times 10^{-3} \frac{n_e}{\nu^2 T^{3/2}} \left(\sum_i Z_i^2 n_i\right) G(T,\nu) \tag{2}$$

where κ_ν is the thermal bremsstrahlung opacity, L is the plasma line-of-sight depth considered, and $G(T,\nu)$ is the Gaunt factor that we obtain numerically from van Hoof et al. (2014). In addition, n_e and n_i are the number densities of free electrons and ions of specie i, respectively, and Z_i is the atomic number of specie i. As we consider a fully ionized, ideal plasma with a solar abundance of 70.7% H + 27.4% He + 1.9% heavier elements (Prialnik, 2000), we infer that $\sum_i Z_i^2 n_i = 3.703n$, with n the average total ion number density, and from which we derive the electron density $n_e = 1.445n$. Ω is the solid angle considered.

From **Eq. 2**, we compute the thermal bremsstrahlung opacities κ_ν as a function of the observing frequency ν for the SADs and fans of models 1–5. **Figure 3** shows the obtained results. Color-continuous lines represent the SAD opacities, while color-dashed

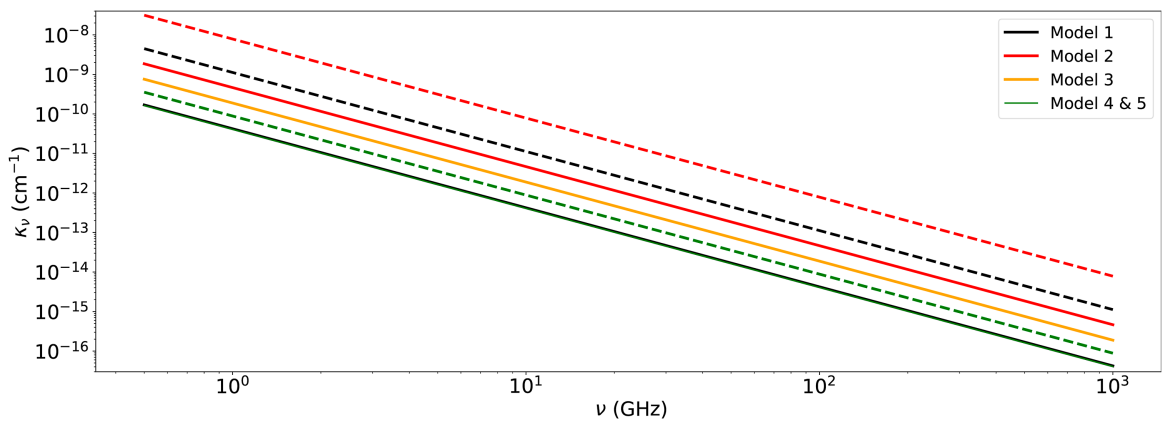

FIGURE 3 | Mean thermal bremsstrahlung opacities κ_ν for the different models (identified by colors) in the frequency range [0.5–1,000] GHz. Continuous lines correspond to inner (SAD) opacities, while dashed lines correspond to outer (fan) opacities. Fan opacities for models 2 and 3 are equal; the same happens for models 4 and 5. It is to be noted that SAD opacities for models 1, 4, and 5 are similar (lowest superimposed continuous lines).

lines represent the corresponding fan opacities, which in general are larger in values. For fans and SADs, the regime should be optically thin greater than 10 GHz. However, in some cases, that will be analyzed later, the transition from optically thick to thin regimes may happen at frequencies below 1 GHz.

We can now estimate the integrated flux density emitted by the whole SAD using **Eq. 1** and the mean values from **Table 1**. The intrinsically inhomogenous dynamics of the fan implies that random fluctuations cancel out when integrated over the line-of-sight, and therefore the use of mean values is appropriate for computing the outgoing radiation observed on Earth. In the calculation, we assume that all sources are cylindrical with a diameter equal to the SAD size, and the solid angle $\Omega = \pi L_{\rm sad}^2/4{\rm AU}^2$, with AU the mean Sun–Earth distance. The chromospheric contribution is not considered because we are considering an observer viewing the fan over the limb. As sketched in **Figure 1**, we assume an observer in the outcoming-radiation direction and that the SAD is embedded in the fan; thus, we consider the fan emission in front of and behind the SAD. Given that we are interested in the contrast, we want to compare the outgoing radiations coming from a direction, including the SAD, with another one just considering the surrounding fan. When the considered direction includes the SAD, a three-layer calculation is carried out (see the inset in **Figure 1**); otherwise, just one layer is considered. For all cases, the layers are assumed isothermal and homogenous. In the three-layer calculation of the flux density, the inner (L_1) and outer (L_3) layers are formed by the fan plasma, whereas the middle layer corresponds to the SAD (L_2). Here, we assume that in general $L_{\rm fan} > L_{\rm sad}$—although there is no conclusive observational data on this detail— and we suppose that the SAD layer is in the geometrical center of the fan, so the depth of the inner and outer layers are defined as $L_{\rm fan}^* = (L_{\rm fan} - L_{\rm sad})/2$. In this case, the final total flux density is then

$$F_{\rm sad}(\nu) = F_{\rm L_1}(\nu) + F_{\rm L_2}(\nu) + F_{\rm L_3}(\nu). \tag{3}$$

The emerging flux density from L_1, after traversing the SAD (L_2) and outer fan (L_3) layers, is

$$F_{\rm L_1}(\nu) = \frac{2k_{\rm B}T_{\rm fan}\nu^2}{c^2}\left(1 - e^{-\tau_{\rm L_1}(\nu)}\right)e^{-\tau_{\rm L_2}(\nu)}e^{-\tau_{\rm L_3}(\nu)}\Omega, \tag{4}$$

where $\tau_{\rm L_1}$, $\tau_{\rm L_2}$, and $\tau_{\rm L_3}$ are the opacities of the layers L_1, L_2, and L_3, respectively. In a similar way, the emerging flux density from the SAD layer is

$$F_{\rm L_2}(\nu) = \frac{2k_{\rm B}T_{\rm sad}\nu^2}{c^2}\left(1 - e^{-\tau_{\rm L_2}(\nu)}\right)e^{-\tau_{\rm L_3}(\nu)}\Omega. \tag{5}$$

Finally, for the outer layer, we have

$$F_{\rm L_3}(\nu) = \frac{2k_{\rm B}T_{\rm fan}\nu^2}{c^2}\left(1 - e^{-\tau_{\rm L_3}(\nu)}\right)\Omega. \tag{6}$$

On the other hand, the emerging radiation when observing the SAD direction has only the fan contribution (a one-layer calculation)

$$F_{\rm fan}(\nu) = \frac{2k_{\rm B}T_{\rm fan}\nu^2}{c^2}\left(1 - e^{-\tau_{\rm fan}(\nu)}\right)\Omega\ , \tag{7}$$

where $\tau_{\rm fan}(\nu)$ is the opacity of the whole fan line-of-sight depth $L_{\rm fan}$.

Figure 4 displays the resulting integrated flux densities and contrasts $Q = F_{\rm fan}(\nu)/F_{\rm sad}(\nu)$, dividing **Eq. 7** by **Eq. 3**. The results are displayed for the edge-on (**Figures 4A,B**) and face-on (**Figures 4C,D**) views of the fan, with line-of-sight depths $L_{\rm fan}$ = 30 Mm and $L_{\rm fan}$ = 5 Mm, respectively. It is to be noted that the flux density is almost constant for frequencies $\nu \gtrsim 5$ GHz, where the spectrum is optically thin. The SAD integrated flux densities $F_{\rm sad}(\nu)$ are in the range $\sim[10^2 - 10^4]$ Jy and are weaker than the fan flux densities $F_{\rm fan}(\nu)$. This is also evident in the right panels where we see contrasts $Q > 1$. Model 3 exhibits the highest contrasts, of 1.6 on the edge-on view and 6 on the face-on view, while model 1 exhibits the lowest, of 1.05 and 1.7, respectively. The remaining contrasts lie between these extremes. When the spectra become optically thick ($\nu \lesssim 5$ GHz), the contrasts tend to conform to unity, particularly in the edge-on view, meaning that the SAD layer contribution to the total flux density is negligible. Interestingly, for model 3 in the face-on view, we see $Q < 1$, implying that the SAD is brighter than the fan.

3.3 Gyroresonance

In the previous calculations of **Section 3.2**, we did consider gyroresonance radiation, an emission mechanism that depends on the magnetic field intensity, in addition to the temperature and density. The gyroresonance opacity at frequency ν depends on the harmonic number $s = \nu/\nu_B$, where $\nu_B = 2.8 \times 10^6 B$, with B the magnetic field intensity in G. The opacity at a given harmonic number τ_s (e.g., Casini et al., 2017) is proportional to $\tau_s \propto \frac{s^2}{s!}$. Because of this dependence, only the very first harmonics produce detectable emission. Indeed, usually, only the first three harmonics are considered (see, e.g., White, 2004; Selhorst et al., 2008). In the present case, where magnetic field intensities of the MHD simulations are $B \leq 14$ G, we have $\nu_B \leq 0.039$ GHz; therefore, for the lowest frequency, $\nu = 0.5$ GHz, $s \geq 13$, and $\tau_s \propto s^2/s! \lesssim 10^{-8}$. Since for higher frequencies the harmonic number s will be even larger, we can neglect the gyroresonance contribution from the emerging flux density in the frequency range [0.5–1,000] GHz used in our calculations.

3.4 2D Synthesized Radio Maps

Here, we use model 1 to synthesize images that we expect to observe with the present radio telescopes. Since model 1 is 2D, we do not include the fan contribution in front of or behind the SAD as was carried out previously in **Section 3.2**; instead, every grid cell is thought of as a homogenous source with a line-of-sight depth L = 5 Mm. This value for the line-of-sight depth is deduced from the fact that model 1 accounts for a fan viewed face-on. The solid angle $\Omega = \delta x^2/{\rm AU}^2$ is considered, which is defined by the grid resolution ($\delta x = \delta y = 5 \times 10^6$ cm) of the simulation. Using **Eq. 1**, we obtain the flux density emitted by every grid cell, and then to simulate observations, the resulting flux map is convolved with representations of instrument beams. In this case, due to the small size of the SAD, an instrument with high spatial resolution is needed to separate the SAD emission from the background

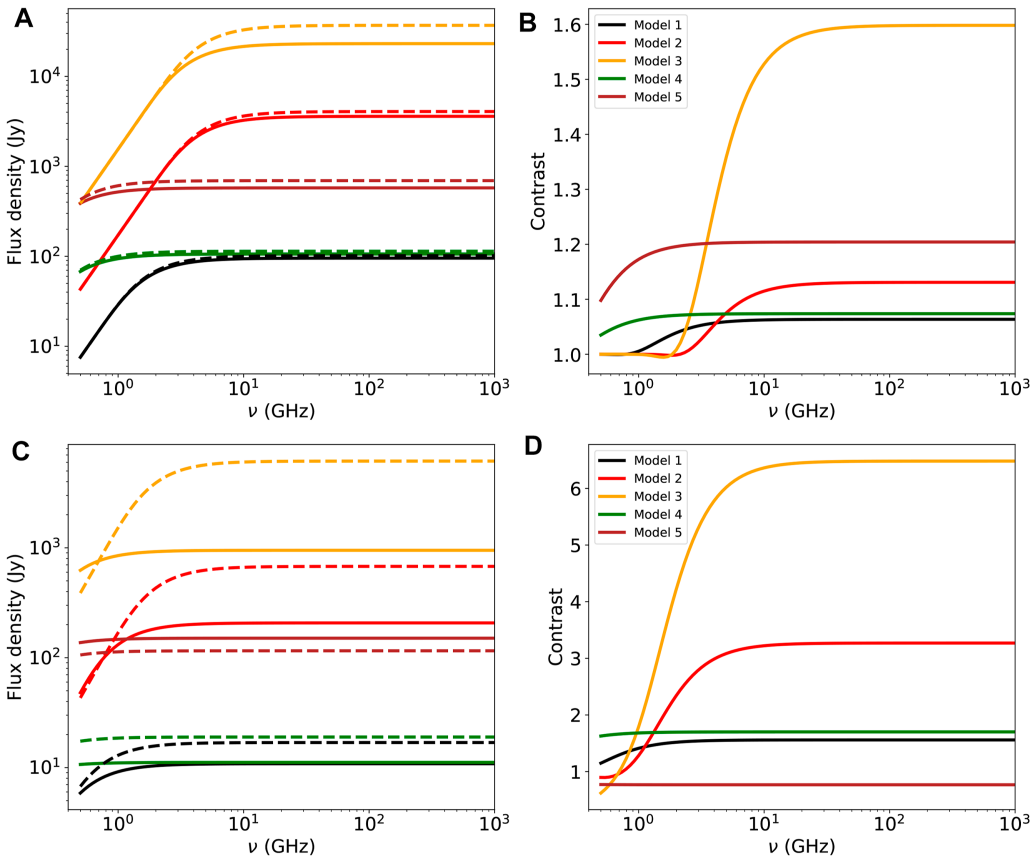

FIGURE 4 | Left panels show the expected flux density spectra incoming from the SADs (continuous lines) and for the fan (dashed lines). Right panels show the fan-SAD contrasts (flux density quotient between the fan and SADs). **(A,B)** Results for the fan viewed edge-on. **(C,D)** Results for the fan viewed face-on.

fan. Nowadays, there are only two instruments with arcsec spatial resolution in radio wavelengths and capable of observing the Sun: the VLA and ALMA. Both are interferometers with synthesized beams of the order of 1 arcsec and sensitivities below 1 mJy.

We compute the emissions for the VLA microwave band S (3 GHz) and also for the ALMA bands: 3 (100 GHz), 6 (230 GHz), and 9 (720 GHz). Since the spectrum is mostly optically thin, and aiming to display results for a low and high frequency in the thermal bremsstrahlung–opacity domain [0.5–1,000] GHz considered in **Figure 3**, we show in **Figure 5** the synthesized maps for the VLA band S at 3 GHz (**Figures 5A,B**) and the ALMA band 3 at 100GHz (**Figures 5C,D**). Left panels represent the flux densities with the simulation grid spatial resolution, while the right panels show the resulting flux densities convolved with the two instrument beams, at the top using the VLA band S with a half-power beamwidth HPBW = 0.65″ and at the bottom using the ALMA band 3 with HPBW = 0.3″. It is to be noted that the fan emission is always brighter than the SAD, with a contrast $Q \approx 6$. On the other hand, the convolved maps depend more on the spatial resolution (instrument beam) than on the flux density. For small SADs, such as that of model 1, using instruments with HPBW > 1″ will result in SADs spatially unresolved from the background fan emission. In terms of sensitivity, the expected flux detected by the instruments is in the order of or above 1 mJy/pixel.

In the 2D scenario, the order of magnitude for the emission contrast Q between the fan and SADs can be estimated straightforwardly in the optically thin regime. As was pointed out previously, the contrast depends on the model considered, for example, for models 1–3, the fan temperatures are roughly half of the SAD ones, whereas the fan densities are roughly twice of the SAD ones. Due to the fact that we are considering the optically thin regime, the opacity $\kappa_\nu \propto n^2 \nu^{-2} T^{-3/2}$ (**Eq. 2**); furthermore, the emission in the Rayleigh–Jeans approximation can be written as $F_\nu \propto T\nu^2 \kappa_\nu L\Omega \equiv n^2 T^{-1/2} L\Omega$; and thus, for these models, we obtain an order-of-magnitude contrast

$$Q = \frac{n_{\rm fan}^2 \; T_{\rm fan}^{-1/2} \; L \; \Omega}{n_{\rm sad}^2 \; T_{\rm sad}^{-1/2} \; L \; \Omega} = \left(\frac{n_{\rm fan}}{n_{\rm sad}}\right)^2 \left(\frac{T_{\rm sad}}{T_{\rm fan}}\right)^{1/2} \simeq 2^2 \cdot 2^{1/2} = 5.6. \quad (8)$$

This number is consistent with the contrast displayed by the flux densities in **Figure 5**. In addition, and as a support to the 2D-scenario results, the approximate contrast of **Eq. 8** is of the same order as that reported by Guo et al. (2014) in their **Figures 2D,E**, where 2D slices of the expected emissions were

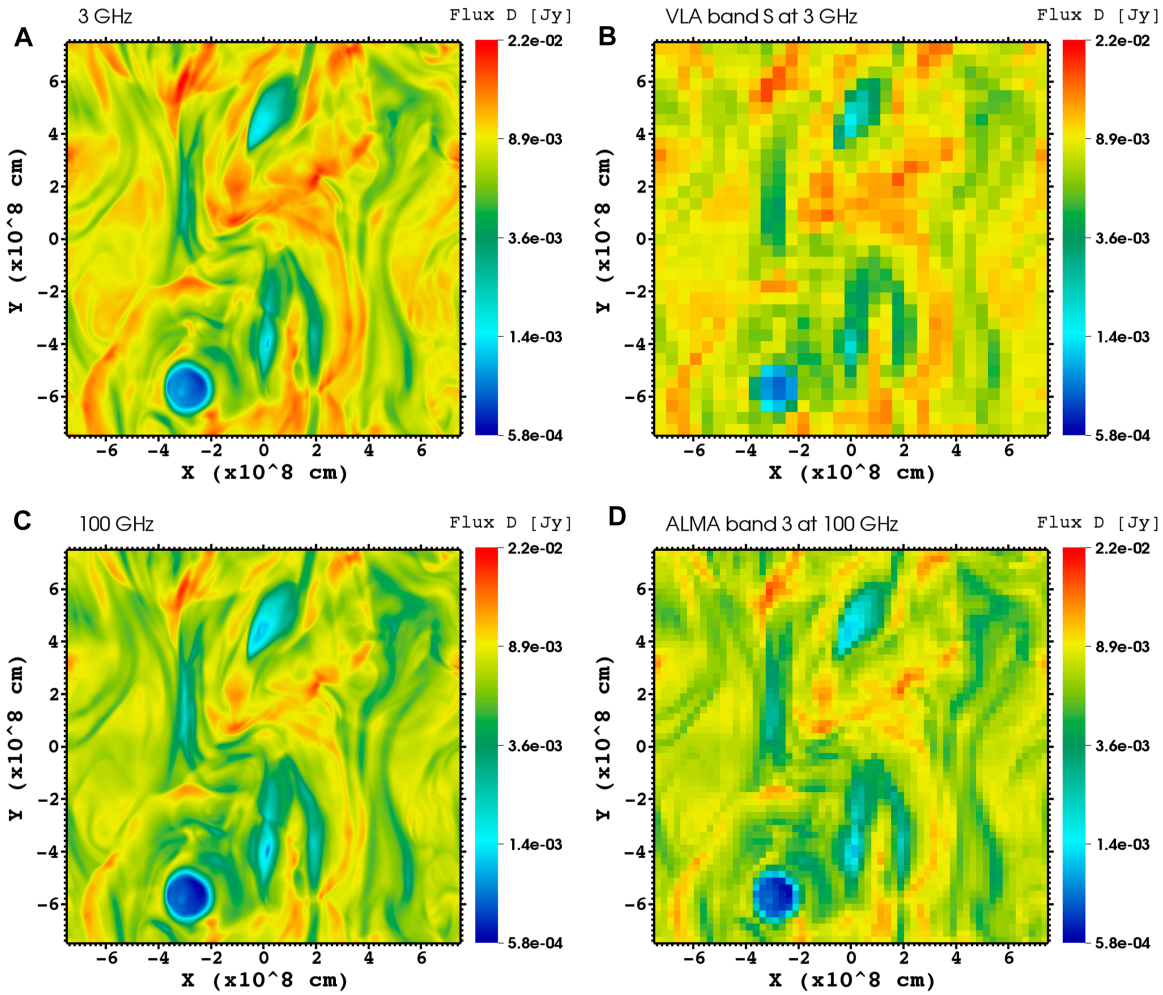

FIGURE 5 | (A) Expected flux density at 3 GHz obtained from an MHD simulation, and the flux density convolved with the VLA-band S beam of HPBW = 0.65″ **(B)**. **(C)** Simulated flux density at 100 GHz and the flux density convolved with the ALMA-band 3 beam of HPBW = 0.3″ **(D)**. It is to be noted that 10^8 cm ≡ 1 Mm.

shown to be corresponding to face-on views of the SDO/AIA Fe XXI and Fe XXIV channels, respectively. Finally, if we repeat the simple contrast calculation of **Eq. 8**, but instead using model 2 (see the 2D slices in density and temperature displayed in Figure 5 by Cécere et al. (2015), we again obtain a similar value. However, the contrast decrease is considerable when the plasma line-of-sight depth is taken into account, as illustrated in **Figure 4**.

3.5 Observational Strategies

It is evident from the flux density spectra displayed in **Figure 4** that observations with edge-on views produce lower contrasts than with face-on views, making SAD detection more difficult, which worsens in the optically thick regime. Since the emission from microwaves to submillimeter wavelengths is mostly optically thin, the best strategy to observe SADs is when the fan line-of-sight is over the dark limb and when the fan is viewed face-on. On the other hand, according to the models analyzed in this work, the spatially integrated flux emitted by SADs (**Figures 4A–C**) can be as low as ≈ 1 Jy and as high as ≈10^3 Jy. This means that a highly sensitive telescope is not required, although imaging capability is needed. The best instrument is an interferometer, for example, VLA has receivers in the low-frequency domain [1–18] GHz, and ALMA has receivers in the high-frequency domain [45–900] GHz. Both the instruments have adequate sensitivity and spatial resolution to observe even the smallest SAD (≈3 arcsec) of model 1, shown in **Figures 2**, **4**, **5**. Therefore, the best strategy would be to observe at different frequencies simultaneously with VLA and ALMA to cover the possible maximum frequency range. Moreover, instruments below the 1-GHz domain, such as Low-Frequency Array (van Haarlem et al., 2013) and Nançay Radioheliograph (Kerdraon and Delouis, 1997), can supply information in the optically thick spectral range, allowing better determination

of the density and temperature of the emitting sources. The Extended Owens Valley Array (EOVSA, Gary et al., 2018), with its spectral imager in [1–18] GHz range, could be used for the biggest SADs since its beam sizes are of the order of $\approx 54/\nu$[GHz]arcsec.

4 FINAL REMARKS

So far, SADs have been elusive structures likely produced by magnetic reconnection processes during solar flares. They have been detected only in EUV and soft X-ray emission, implying that currently known SAD characteristics, such as their temperatures, densities, and sizes, have been inferred using this wavelength range. The same thermal bremsstrahlung phenomenon that produces emission in EUV and soft X-ray should also produce emission in radio wavelengths. However, no direct observation of SADs in radio has been reported yet. Instead, in radio only were reported signatures of magnetic reconnection processes assumed to be responsible for SAD triggering, and also spatial/temporal correlations of SAD signatures with a burst of impulsive microwave emissions. Thus, the use of radio observations for SAD detection may help improve the estimations of SAD characteristics.

In order to contribute to the understanding of SAD nature, in this study, we produced spatially integrated spectra and synthesized images at selected radio frequencies. The spectra were obtained utilizing numerical MHD models of SADs based on the bursty localized reconnection interpretation by Costa et al. (2009) and subsequent works and the reconnection downflow interpretation by Guo et al. (2014). Here, we demonstrated that the fan emission should be detectable with current radio observatories and that the SADs should consistently be less bright than the surrounding fan. In the frequency range analyzed, [0.5–1,000] GHz, the spectra of SADs and fans show that the thermal bremsstrahlung emission greater than 10 GHz is mostly optically thin, and therefore proportional to the temperature, density, and line-of-sight depth. Furthermore, the gyroresonance contribution to the flux density is negligible. The fan emission and SAD sizes have a strong influence in their measured contrast Q. The contrast is a parameter that describes the detectability of a SAD, meaning that it is indistinguishable from the ambient-fan emission when it is close to unity. The fact that the contrast is not sufficiently high may be a reason why SADs are barely detected during eruptive events, particularly when the fan is viewed edge-on (as shown in **Figure 4**).

Despite our results being model-dependent, a strategic plan to increase chances of SAD detection in radio wavelengths is to first search for post-flare magnetic arcades over the limb, where a face-on view of the fan will be mostly desired; and second, to simultaneously observe at centimeter and millimeter wavelengths. Imaging SADs with arcsec resolution simultaneously at different radio wavelengths would be an excellent diagnostic to constraint models, with the VLA and ALMA interferometers being the best instruments to achieve this goal. Moreover, a combination of radio, EUV, and soft X-ray observations will enrich the description and deepen our understanding of the physical processes.

It is known that magnetic reconnection is in the origin of a great variety of phenomena: flares, CMEs, etc. Some of these phenomena are weak and, therefore, difficult to detect, as is the case with SADs. The SAD models used in this work consider that magnetic reconnection occurs at coronal heights, which is in line with the above-the-looptop hard X-ray source scenario (also known as Masuda flares, Masuda et al., 1994; Krucker et al., 2008) In order to fully understand the reconnection process and its consequences, we need to complete the SAD picture. Radio observations can be a key to having a more detailed image of them.

DATA AVAILABILITY STATEMENT

The original contributions presented in the study are included in the article/Supplementary Material, further inquiries can be directed to the corresponding author.

AUTHOR CONTRIBUTIONS

EZ, CC, and MC contributed to the conception and design of the study. CC carried out the analytical calculations, EZ performed the synthetic images, and CS assessed the radio emission mechanisms. AC contributed to the model and result discussions. EZ and CC led the manuscript writing. All the authors contributed to manuscript revision and read and approved the submitted version.

FUNDING

The research leading to these results has received funding from CAPES grant 88881.310386/2018-01, FAPESP grant 2013/24155-3. EZ, AC, and MC acknowledge support by CONICET grant number PIP No. 11220200103150CO.

ACKNOWLEDGMENTS

EZ is grateful to the FAPESP to have financed this research by the grant 2018/25177-4. GC thanks CNPq for support with a Productivity Research Fellowship. The authors are also grateful to Mackenzie Research Funding Mackpesquisa for the received support. GC is correspondent researcher of the Consejo Nacional de Investigaciones Científicas y Técnicas (CONICET) for the Instituto de Astronomía y Física del Espacio (IAFE), Argentina. MC and AC are members of the Carrera del Investigador Científico (CONICET). MC acknowledges support from ANPCyT under the grant PICT No. 2016-2480. MC also acknowledges support from the SECYT-UNC grant no. 33620180101147CB. We also thank the VisIt team–graphical tool (Harrison and Krishnan, 2012). The authors thank the editor and the referees for valuable and constructive comments and suggestions that helped improving this work significantly.

REFERENCES

Asai, A., Yokoyama, T., Shimojo, M., and Shibata, K. (2004). Downflow Motions Associated with Impulsive Nonthermal Emissions Observed in the 2002 July 23 Solar Flare. *ApJ* 605, L77–L80. doi:10.1086/420768

Cai, Q., Shen, C., Raymond, J. C., Mei, Z., Warmuth, A., Roussev, I. I., et al. (2019). Investigations of a Supra-arcade Fan and Termination Shock above the Top of the Flare-Loop System of the 2017 September 10 Event. *Mon. Not. Roy. Astron. Soc.* 489, 3183–3199. doi:10.1093/mnras/stz2167

Casini, R., White, S. M., and Judge, P. G. (2017). Magnetic Diagnostics of the Solar Corona: Synthesizing Optical and Radio Techniques. *Space Sci. Rev.* 210, 145–181. doi:10.1007/s11214-017-0400-6

Cécere, M., Schneiter, M., Costa, A., Elaskar, S., and Maglione, S. (2012). Simulation of Descending Multiple Supra-arcade Reconnection Outflows in Solar Flares. *ApJ* 759, 79. doi:10.1088/0004-637X/759/2/79

Cécere, M., Zurbriggen, E., Costa, A., and Schneiter, M. (2015). 3D MHD Simulation of Flare Supra-Arcade Downflows in a Turbulent Current Sheet Medium. *ApJ* 807, 6. doi:10.1088/0004-637X/807/1/6

Chen, B., Bastian, T. S., Shen, C., Gary, D. E., Krucker, S., and Glesener, L. (2015). Particle Acceleration by a Solar Flare Termination Shock. *Science* 350, 1238–1242. doi:10.1126/science.aac8467

Chen, X., Liu, R., Deng, N., and Wang, H. (2017). Thermodynamics of Supra-arcade Downflows in Solar Flares. *A&A* 606, A84. doi:10.1051/0004-6361/201629893

Costa, A., Elaskar, S., Fernandez, C. A., and Martinez, G. (2009). Simulation of Dark Lanes in post-flare Supra-arcade. *Mon. Not. Roy. Astron. Soc.* 400, L85–L89. doi:10.1111/j.1745-3933.2009.00769.x

Dulk, G. A. (1985). Radio Emission from the Sun and Stars. *Annu. Rev. Astron. Astrophys.* 23, 169–224. doi:10.1146/annurev.aa.23.090185.001125

Freed, M. S., and McKenzie, D. E. (2018). Quantifying Turbulent Dynamics Found within the Plasma Sheets of Multiple Solar Flares. *ApJ* 866, 29. doi:10.3847/1538-4357/aadee4

Gary, D. E., Chen, B., Dennis, B. R., Fleishman, G. D., Hurford, G. J., and Krucker, S. (2018). Microwave and Hard X-Ray Observations of the 2017 September 10 Solar Limb Flare. *Astrophys. J.* 863, 83. doi:10.3847/1538-4357/aad0ef

Guo, L. J., Huang, Y., Bhattacharjee, A., and Innes, D. E. (2014). Rayleigh-Taylor Type Instabilities in the Reconnection Exhaust Jet as a Mechanism for Supra-arcade Downflows in the Sun. *Astrophys. J. Lett.* 796, L29. doi:10.1088/2041-8205/796/2/l29

Hanneman, W. J., and Reeves, K. K. (2014). Thermal Structure of Current Sheets and Supra-arcade Downflows in the Solar Corona. *Astrophys. J.* 786, 95. doi:10.1088/0004-637X/786/2/95

Harrison, C., and Krishnan, H. (2012). "Python's Role in VisIt," in *11th Python in Science Conf. (Scipy 2012)*. Editors Ahmadia, A., Millman, J., and van der, S., 23–29. doi:10.25080/Majora-54c7f2c8-00d

Hayes, L. A., Gallagher, P. T., Dennis, B. R., Ireland, J., Inglis, A., and Morosan, D. E. (2019). Persistent Quasi-Periodic Pulsations during a Large X-Class Solar Flare. *Astrophys. J.* 875, 33. doi:10.3847/1538-4357/ab0ca3

Innes, D. E., Guo, L. J., Bhattacharjee, A., Huang, Y. M., and Schmit, D. (2014). Observations of Supra-arcade Fans: Instabilities at the Head of Reconnection Jets. *Astrophys. J.* 796, 27. doi:10.1088/0004-637X/796/1/27

Innes, D. E., McKenzie, D. E., and Wang, T. (2003a). Observations of 1000 Km S^{-1} Doppler Shifts in 10^7 K Solar Flare Supra-arcade. *Solar Phys.* 217, 267–279. doi:10.1023/b:sola.0000006874.31799.bc

Innes, D. E., McKenzie, D. E., and Wang, T. (2003b). SUMER Spectral Observations of post-flare Supra-arcade Inflows. *Solar Phys.* 217, 247–265. doi:10.1023/b:sola.0000006899.12788.22

Kerdraon, A., and Delouis, J.-M. (1997). "The Nançay Radioheliograph," in *Coronal Physics from Radio and Space Observations*. Editor Trottet, G. (Springer Berlin Heidelberg), 192–201. doi:10.1007/BFb0106458

Krucker, S., Battaglia, M., Cargill, P. J., Fletcher, L., Hudson, H. S., MacKinnon, A. L., et al. (2008). Hard X-ray Emission from the Solar corona. *Astron. Astrophys. Rev.* 16, 155–208. doi:10.1007/s00159-008-0014-9

Li, Z. F., Cheng, X., Ding, M. D., Reeves, K. K., Kittrell, D., Weber, M., et al. (2021). Thermodynamic Evolution of Solar Flare Supra-arcade Downflows. *Astrophys. J.* 915, 124. doi:10.3847/1538-4357/ac043e

Linton, M. G., Devore, C. R., and Longcope, D. W. (2009). Patchy Reconnection in a Y-type Current Sheet. *Earth, Planets, and Space* 61, 573–576. doi:10.1186/bf03352925

Linton, M. G., and Longcope, D. W. (2006). A Model for Patchy Reconnection in Three Dimensions. *Astrophys. J.* 642, 1177–1192. doi:10.1086/500965

Liu, R. (2013). Dynamical Processes at the Vertical Current Sheet behind an Erupting Flux Rope. *Mon. Not. Roy. Astron. Soc.* 434, 1309–1320. doi:10.1093/mnras/stt1090

Liu, W., Chen, Q., and Petrosian, V. (2013). Plasmoid Ejections and Loop Contractions in an Eruptive M7.7 Solar Flare: Evidence of Particle Acceleration and Heating in Magnetic Reconnection Outflows. *Astrophys. J.* 767, 168. doi:10.1088/0004-637X/767/2/168

Longcope, D., Unverferth, J., Klein, C., McCarthy, M., and Priest, E. (2018). Evidence for Downflows in the Narrow Plasma Sheet of 2017 September 10 and Their Significance for Flare Reconnection. *Astrophys. J.* 868, 148. doi:10.3847/1538-4357/aaeac4

Longcope, D. W., Guidoni, S. E., and Linton, M. G. (2009). Gas-dynamic Shock Heating of Post-flare Loops Due to Retraction Following Localized, Impulsive Reconnection. *Astrophys. J. Lett.* 690, L18–L22. doi:10.1088/0004-637x/690/1/l18

Maglione, L. S., Schneiter, E. M., Costa, A., and Elaskar, S. (2011). Simulation of Dark Lanes in post-flare Supra-arcades. III. A 2D Simulation. *Astron. Astrophys.* 527, L5. doi:10.1051/0004-6361/201015934

Masuda, S., Kosugi, T., Hara, H., Tsuneta, S., and Ogawara, Y. (1994). A Loop-Top Hard X-ray Source in a Compact Solar Flare as Evidence for Magnetic Reconnection. *Nature* 371, 495–497. doi:10.1038/371495a0

McKenzie, D. E., and Hudson, H. S. (1999). X-Ray Observations of Motions and Structure above a Solar Flare Arcade. *Astrophys. J. Lett.* 519, L93–L96. doi:10.1086/312110

McKenzie, D. E., and Savage, S. L. (2011). Distribution Functions of Sizes and Fluxes Determined from Supra-arcade Downflows. *Astrophys. J. Lett.* 735, L6. doi:10.1088/2041-8205/735/1/L6

McKenzie, D. E., and Savage, S. L. (2009). Quantitative Examination of Supra-arcade Downflows in Eruptive Solar Flares. *Astrophys. J.* 697, 1569–1577. doi:10.1088/0004-637X/697/2/1569

McKenzie, D. E. (2013). Turbulent Dynamics in Solar Flare Sheet Structures Measured with Local Correlation Tracking. *Astrophys. J.* 766, 39. doi:10.1088/0004-637X/766/1/39

Prialnik, D. (20002000). *An Introduction to the Theory of Stellar Structure and Evolution*". Cambridge: University Press. doi:10.1080/00107514.2011.580371

Reeves, K. K., Freed, M. S., McKenzie, D. E., and Savage, S. L. (2017). An Exploration of Heating Mechanisms in a Supra-arcade Plasma Sheet Formed after a Coronal Mass Ejection. *Astrophys. J.* 836, 55. doi:10.3847/1538-4357/836/1/55

Savage, S. L., and McKenzie, D. E. (2011). Quantitative Examination of a Large Sample of Supra-arcade Downflows in Eruptive Solar Flares. *Astrophys. J.* 730, 98. doi:10.1088/0004-637X/730/2/98

Savage, S. L., McKenzie, D. E., and Reeves, K. K. (2012). Re-interpretation of Supra-arcade Downflows in Solar Flares. *Astrophys. J. Lett.* 747, L40. doi:10.1088/2041-8205/747/2/L40

Schulz, W., Costa, A., Elaskar, S., and Cid, G. (2010). Simulation of Dark Lanes in post-flare Supra-arcades - II. A Contribution to the Remote Sensing of the Coronal Magnetic Field. *Mon. Not. Roy. Astron. Soc.* 407, L89–L93. doi:10.1111/j.1745-3933.2010.00911.x

Scott, R. B., Longcope, D. W., and McKenzie, D. E. (2013). Peristaltic Pumping Near Post-coronal Mass Ejection Supra-arcade Current Sheets. *Astrophys. J.* 776, 54. doi:10.1088/0004-637X/776/1/54

Selhorst, C. L., Silva-Válio, A., and Costa, J. E. R. (2008). Solar Atmospheric Model over a Highly Polarized 17 GHz Active Region. *Astron. Astrophys.* 488, 1079–1084. doi:10.1051/0004-6361:20079217

van Haarlem, M. P., Wise, M. W., Gunst, A. W., Heald, G., McKean, J. P., Hessels, J. W. T., et al. (2013). LOFAR: The LOw-Frequency ARray. *Astron. Astrophys.* 556. doi:10.1051/0004-6361/201220873

van Hoof, P. A. M., Williams, R. J. R., Volk, K., Chatzikos, M., Ferland, G. J. Lykins, M., et al. (2014). Accurate Determination of the Free-free Gaunt Factor - I. Non-relativistic Gaunt Factors. *Mon. Not. Roy. Astron. Soc.* 444, 420–428. doi:10.1093/mnras/stu1438

Verwichte, E., Nakariakov, V. M., and Cooper, F. C. (2005). Transverse Waves in a post-flare Supra-arcade. *Astron. Astrophys.* 430, L65–L68. doi:10.1051/0004-6361:200400133

Warren, H. P., Brooks, D. H., Ugarte-Urra, I., Reep, J. W., Crump, N. A., and Doschek, G. A. (2018). Spectroscopic Observations of Current Sheet

Formation and Evolution. *Astrophys. J.* 854, 122. doi:10.3847/1538-4357/aaa9b8

Warren, H. P., O'Brien, C. M., Sheeley, J., and Neil, R. (2011). Observations of Reconnecting Flare Loops with the Atmospheric Imaging Assembly. *Astrophys. J.* 742, 92. doi:10.1088/0004-637X/742/2/92

White, S. M. (2004). "Coronal Magnetic Field Measurements through Gyroresonance Emission,". *Astrophysics and Space Science Library*. Editors Gary, D. E., and Keller, C. U., 314, 89. doi:10.1007/1-4020-2814-8_5

Xue, J., Su, Y., Li, H., and Zhao, X. (2020). Thermodynamical Evolution of Supra-arcade Downflows. *Astrophys. J.* 898, 88. doi:10.3847/1538-4357/ab9a3d

Yu, S., Chen, B., Reeves, K. K., Gary, D. E., Musset, S., Fleishman, G. D., et al. (2020). Magnetic Reconnection during the Post-impulsive Phase of a Long-Duration Solar Flare: Bidirectional Outflows as a Cause of Microwave and X-Ray Bursts. *Astrophys. J.* 900, 17. doi:10.3847/1538-4357/aba8a6

Zurbriggen, E., Costa, A., Esquivel, A., Schneiter, M., and Cécere, M. (2016). MHD Simulations of Coronal Supra-arcade Downflows Including Anisotropic Thermal Conduction. *Astrophys. J.* 832, 74. doi:10.3847/0004-637X/832/1/74

Conflict of Interest: The authors declare that the research was conducted in the absence of any commercial or financial relationships that could be construed as a potential conflict of interest.